



UNIVERSITY OF LEEDS

This is a repository copy of *Effect of Flow Rate on the Corrosion Behavior of API 5L X80 Steel in Water-Saturated Supercritical CO2 Environments*.

White Rose Research Online URL for this paper:

<https://eprints.whiterose.ac.uk/203964/>

Version: Accepted Version

---

**Article:**

da Silva de Sá, J., Ma, W., Owen, J. [orcid.org/0000-0003-0778-0858](https://orcid.org/0000-0003-0778-0858) et al. (4 more authors) (Cover date: 1 January 2022) *Effect of Flow Rate on the Corrosion Behavior of API 5L X80 Steel in Water-Saturated Supercritical CO2 Environments*. *Corrosion*, 78 (1). pp. 58-67. ISSN 0010-9312

<https://doi.org/10.5006/3939>

---

© 2022, AMPP. This is an author produced version of an article published in *CORROSION*. Uploaded in accordance with the publisher's self-archiving policy.

**Reuse**

Items deposited in White Rose Research Online are protected by copyright, with all rights reserved unless indicated otherwise. They may be downloaded and/or printed for private study, or other acts as permitted by national copyright laws. The publisher or other rights holders may allow further reproduction and re-use of the full text version. This is indicated by the licence information on the White Rose Research Online record for the item.

**Takedown**

If you consider content in White Rose Research Online to be in breach of UK law, please notify us by emailing [eprints@whiterose.ac.uk](mailto:eprints@whiterose.ac.uk) including the URL of the record and the reason for the withdrawal request.



[eprints@whiterose.ac.uk](mailto:eprints@whiterose.ac.uk)  
<https://eprints.whiterose.ac.uk/>

# Effect of flow rate on the corrosion behaviour of API 5L X80 steel in water-saturated supercritical CO<sub>2</sub> environments

Jonas da Silva de Sá<sup>\*,\*\*</sup>, Wenlong Ma<sup>\*\*,\*\*\*</sup>, Joshua Owen<sup>\*\*</sup>, Yong Hua<sup>\*\*</sup>, Anne Neville<sup>\*\*</sup>, José A. C. Ponciano Gomes<sup>\*</sup>, Richard Barker<sup>\*\*</sup>

\*Corresponding author. E-mail: jonas.sa@coppe.ufrj.br

\*Metallurgical and Materials Engineering Program, Federal University of Rio de Janeiro, Rio de Janeiro, 21941-598, Brazil.

\*\*School of Mechanical Engineering, University of Leeds, Leeds, LS2 9JT, United Kingdom.

\*\*\*School of Mechanical and Electronic Engineering, China University of Petroleum, Qingdao, 266580, PR China.

## **ABSTRACT**

The effect of the water-saturated supercritical carbon dioxide (scCO<sub>2</sub>) flow rate on the corrosion behaviour of API 5L X80 steel at a temperature of 35 °C and pressure of 80 bar was investigated. Tests were carried out with the samples attached to a rotating shaft inside an autoclave. Results indicate that increasing the scCO<sub>2</sub> flow rate had no significant influence on the general/localized corrosion rate under the various dynamic conditions considered. The average general corrosion rate was 0.064 mm/year, while the average measured pitting penetration rates were one order of magnitude higher. The size of the corrosion features on the surface of the samples, which were believed to provide an indication as to the size of the condensed water droplets, were much smaller than the calculated critical droplet size needed to be displaced by the flow, supporting the theory as to why flow rate had little effect on the corrosion response.

**KEY WORDS:** *steel, supercritical environment, carbon dioxide, flow effects.*

## **1 INTRODUCTION**

Global warming has become a wide public concern, with CO<sub>2</sub> emission into the atmosphere representing one of the biggest contributors to the rise in the Earth's temperature. Carbon capture and storage (CCS) technology is currently a feasible and economic method for reducing greenhouse gases emissions. It consists of capturing CO<sub>2</sub> from large source points, compressing it into a liquid or supercritical state and transporting it to a storage site for sequestration or for the purposes of enhanced oil recovery (EOR) [1]. Hence, the implementation of CCS technologies has the potential to reduce CO<sub>2</sub> emissions into the atmosphere, whilst also facilitating the recovery of hydrocarbons through the application [2]. The handling of CO<sub>2</sub> during CCS needs to be conducted in a safe manner; therefore, it is essential to evaluate the corrosion risk in CO<sub>2</sub> transport and injection pipelines [3,4].

Although dry CO<sub>2</sub> is not corrosive to steels, the presence of free water has been regarded as a particular cause for concern for supercritical CO<sub>2</sub> applications. If water is present, it quickly becomes saturated with CO<sub>2</sub>, producing carbonic acid, thus creating a local corrosive environment that may affect the pipeline integrity [3]. Therefore, most applications focus on sufficiently drying the CO<sub>2</sub> before using it. However, in water-alternating-gas (WAG) EOR applications, the well is flooded alternatively with CO<sub>2</sub> and water, in such applications residual water cannot be avoided and the injection lines would be periodically exposed to CO<sub>2</sub> fluids with different water contents [1].

The effect of water content, impurities, temperature, pressure, on the corrosion of the steel in static supercritical CO<sub>2</sub> has been extensively studied in recent years [3,5]. However, the effect of flow rate on the supercritical CO<sub>2</sub> corrosion behaviour of the steel has rarely been reported. It has been shown that in the specific aqueous phase environments, the corrosion rate of the steel can increase substantially due to the mass-transfer generated by the flow. The increase in local turbulence in aqueous environments can also hinder the formation or damage the protective corrosion products film on the surface [6,7].

However, in the supercritical CO<sub>2</sub> phase, the corrosion mechanism is substantially different to that encountered in a single-phase flow aqueous environment, and more akin to corrosion in condensate/wet-gas systems. In this scenario, the water can locally exceed the solubility limit and condense via a dropwise or film-wise mechanisms onto the steel surface, leading to corrosion of the area in direct contact with the aqueous phase [8]. The corrosion in such systems is expected to be controlled by the electrochemical reaction occurring at the interface between the steel sample and the free water. Consequently, the corrosion rate measured would be influenced by the extent of the wetted area [1,8,9]. Therefore, understanding this initial stage of the condensation process is very important for the prediction of the extent of corrosion in CO<sub>2</sub> injection wells. However, the condensation of water droplets in the supercritical CO<sub>2</sub> phase is still not fully understood. Some authors believe the water droplets condense directly on the steel surface similarly to atmospheric corrosion [10]. While others believe that a variation of temperature or pressure is required for the condensation [11]. A third option is related to the water condensing in the bulk supercritical CO<sub>2</sub> phase to create an emulsion where the droplets would eventually hit and adhere to the steel surface [1].

Any water droplet condensing on the surface would also be subjected to the drag forces exerted by the flowing fluid, creating the potential for it to move along in the flow direction, continuously sweeping other droplets in its path or falling due to gravity, similar to top-of-the-line corrosion mechanisms [12]. However, it should also be noted that corrosion in supercritical CO<sub>2</sub> fluids may be different from that observed in natural gas pipelines, since in some instances there can be a significantly smaller difference between the densities of the two fluids involved that may affect the water-in-sccO<sub>2</sub> emulsion stability [1,13].

This study aims to provide an understanding of the flow effect on the corrosion behaviour of X80 steel in water-saturated supercritical CO<sub>2</sub> phase. Additionally, computational fluid dynamics (CFD) analysis was used to determine the relationship between the hydrodynamics of the fluid droplets within a supercritical CO<sub>2</sub> system and the corrosion behaviour observed.

## **2 EXPERIMENTAL PROCEDURES**

### ***2.1 Material***

The material used in this study was X80 steel with a ferrite-pearlite microstructure and a chemical composition of: 0.041%C, 1.56%Mn, 0.010%P, 0.001%S, 0.300%Si, 0.251%Ni, 0.057%Cr, 0.201%Mo, 0.001%V, 0.037%Nb and Fe balanced. Each test was carried out using six 22 x 9 x 3 mm<sup>3</sup> samples (a 2 mm diameter hole was drilled for mounting) with all surfaces ground progressively following 220, 400 and 800 grit silicon carbide paper. The samples were degreased with acetone, washed with deionised water, and dried before weighing using an electronic balance with an accuracy of 0.01 mg and then stored in a desiccator until use.

### ***2.2 Mass loss measurements***

Tests were performed in a 1 L Hastelloy C276 rotating autoclave. In each test, six samples were fixed in a PEEK sample holder that was then fixed onto a shaft which is able to rotate inside the autoclave, as shown in Figure 1. The experimental conditions are listed in Table 1. Tests

were carried out in static and dynamic conditions in water-saturated scCO<sub>2</sub>. Previous analysis by Spycher et al. [14] indicates that the saturation limit of water in supercritical CO<sub>2</sub> at 35 °C and 80 bar is 3437 ppm. However, to ensure complete saturation of supercritical CO<sub>2</sub>, 10 mL of solution was introduced in the bottom of the autoclave, without direct contact with the samples. Once saturated with CO<sub>2</sub>, the solution was transferred into the autoclave using a pipette, then the autoclave was pressurised up to 30 bar and vented twice to purge any remaining oxygen. After that the autoclave was pressurised to 80 bar using CO<sub>2</sub> and heated to a temperature of 35 °C.

At the end of each test, the autoclave was depressurised before removing the samples, rinsing with deionized water and drying with compressed air. Subsequently samples were weighed, then chemically cleaned with the aid of Clarke's solution (20 g antimony trioxide, 50 g stannous chloride and 1000 ml hydrochloric acid) to remove corrosion products, followed by rinsing with deionized water and drying with compressed air, before weighing again. The average corrosion rate was determined using Eq. (1), as described in ASTM Standard G1 [15], where  $\Delta m$  is the mass difference in g,  $\rho$  is the material density in g/cm<sup>3</sup>,  $A$  is the sample surface area in cm<sup>2</sup>,  $t$  is the test duration in hours and  $C_{rate}$  is the corrosion rate in mm/year.

$$C_{rate} = \frac{87600\Delta m}{\rho A t} \quad (1)$$

### 2.3 Surface analysis

The surface morphology of each sample after the tests was observed using a Carl Zeiss EVO MA15 scanning electron microscope (SEM) to investigate the resulting surface features after corrosion in these conditions. The micrographs were captured using secondary electron mode at an accelerating voltage of 20 kV and at an average working distance of 8 mm. Samples were stored under vacuum in a desiccator prior to the completion of surface analysis.

Due to the number of features observed on each SEM image, ImageJ [16] version 1.53c software was used to process the images allowing a statistical analysis of the size distribution of corrosion patches on the surface. Figure 2 shows the steps used in the analysis. First the corrosion features were manually selected (Figure 2b), then the background was removed, leaving only the selected areas (Figure 2c) and then the software was used for automatic object counting and measuring (Figure 2d).

To determine the extent of localised corrosion, pitting detection and analysis was completed using a non-contact profilometer (NPFLEX 3D Surface Metrology System) across the sample surface, after removing the corrosion products. On each sample, three 1x1 mm<sup>2</sup> sample areas were scanned, which were then used to estimate characteristics of the whole surface. The pit penetration rate was calculated using Eq. (2) [17], where  $C_{pit}$  is the pit penetration rate in mm/year,  $h$  is the pit depth in  $\mu\text{m}$ , and  $t$  is the exposure time in hours.

$$C_{pit} = \frac{8.76h}{t} \quad (2)$$

### 2.4 Computational fluid dynamics (CFD) model

CFD models were used to simulate the fluid flow, allowing the identification of conditions that may affect either the corrosion kinetics or the droplet retention process on the surface of the specimens inside the rotating autoclave test cell [18]. An incompressible, steady-state and isoviscous flow is governed by the following Navier-Stokes equations, where Eq. (3) and (4) represent the conservation of mass and momentum respectively;  $u$  is the flow velocity field,  $p$  is the hydrostatic pressure field,  $\rho$  is the fluid density,  $\mu$  is the fluid viscosity and  $f$  are the external forces,

such as gravity. However, to solve turbulent flows ( $Re > 10^4$ ) Reynolds-Averaged Navier-Stokes (RANS) equations are used, where each variable of the Navier-Stokes equation is split into a mean ( $\underline{u}$ ) plus a turbulent fluctuation ( $u^0$ ) components ( $u = \underline{u} + u^0$ ) [19,20].

$$\nabla \cdot \mathbf{u} = 0 \quad (3)$$

$$\rho(\nabla \cdot \mathbf{u})\mathbf{u} - \mu \nabla^2 \mathbf{u} + \nabla p = \mathbf{f} \quad (4)$$

RANS equations can be solved numerically using a suitable turbulence model. COMSOL Multiphysics® version 5.4 [18] was used to create the simulation and solve for the flow of fluid within the autoclave. The k- $\epsilon$  turbulence model was selected to numerically solve the turbulent fluid flow due to its good convergence rate and relatively low memory requirements. It is a two-equation model that solves for two variables: k, the turbulence kinetic energy (Eq. 5); and the rate of dissipation of turbulence kinetic energy (Eq. 6) [18–20]. Besides that, the local shear stress acting on the sample surface was also obtained by Eq. (7). The 3D model employed a rotating frame (sample holders, samples and shaft), and a stationary container (wall) replicating the dimensions of the experimental setup, as demonstrated in Figure 3a. As the water content in the experiments is much smaller than the volume of CO<sub>2</sub>, the fluid was modelled as single-phase flow.

$$\rho \frac{\partial k}{\partial t} + \rho \mathbf{u} \cdot \nabla k = \nabla \cdot \left( \left( \mu + \frac{\mu_T}{\sigma_k} \right) \nabla k \right) + P_k - \rho \epsilon \quad (5)$$

$$\rho \frac{\partial \epsilon}{\partial t} + \rho \mathbf{u} \cdot \nabla \epsilon = \nabla \cdot \left( \left( \mu + \frac{\mu_T}{\sigma_\epsilon} \right) \nabla \epsilon \right) + C_{\epsilon 1} \frac{\epsilon}{k} P_k - C_{\epsilon 2} \rho \frac{\epsilon^2}{k} \quad (6)$$

$$u_\tau = \sqrt{\frac{\tau_w}{\rho}} \quad (7)$$

### 2.4.1 Boundary conditions

A summary of the boundary conditions used are shown in Figure 3b. A no-slip condition ( $u = 0$ ) was applied at the autoclave walls, sample holder, samples and shaft. A flow continuity was applied to the boundary between the rotating and static domains. The rotating speed was set to either 90, 180, 300 or 600 rpm, to achieve the flow velocities shown in Table 1.

The simulations assumed an incompressible fluid flow (speed of the flow is much smaller than the speed of sound) with density,  $\rho$ , of 524.6 kg/m<sup>3</sup> [21] and dynamic viscosity,  $\mu$ , of  $2.9 \times 10^{-5}$  Pa·s [22], used to replicate the supercritical CO<sub>2</sub> at a temperature of 35 °C and pressure of 80 bar. It was also assumed there were no mechanical vibrations of the apparatus.

### 2.4.2 Model mesh

The k- $\epsilon$  model uses wall functions to solve the fluid flow adjacent to the wall. Wall functions ignore the flow field in the buffer region and analytically compute a fluid velocity at the wall [20]. In order to achieve accurate results using wall functions a finer mesh was used adjacent to the walls to ensure that the dimensionless wall distance is appropriate (i.e.,  $y^+ < 11.06$ ) so that the first node falls outside the boundary layer region.

[18]

Tetrahedral elements were used for the bulk fluid flow domain and prismatic boundary elements were used adjacent to the wall (Figure 4a). A mesh sensitivity analysis was carried out to investigate the compromise between accuracy and computational cost. Figure 4b shows that the

predicted velocity 0.5 mm ahead of the sample leading surface ( $u_{\text{leading}}$ ) did not change significantly after increasing the number of elements used in the mesh past 231,408. Therefore, such mesh resolution was deemed suitable, since the extra computational cost associated with the increasing the mesh density would not affect significantly the predicted results.

### **3 RESULTS AND DISCUSSION**

#### ***3.1 Computational fluid dynamic analysis***

Figure 5 shows the fluid velocity field results at various rotating speeds. In this design the highest velocity occurs near the samples whilst maintaining low velocity fields near the vessel walls and bottom of the autoclave. High velocity fields near the free water resting at the bottom of the autoclave can create local turbulence, resulting in splashing of water droplets that could be dragged by the flow and eventually hit the samples, which is not desired, so this setup was appropriate.

The high velocity fields between two adjacent samples can create a shielding effect [23] such that the opposing surfaces of the sample are exposed to distinct fluid flow conditions. So, it was decided to consider only the surface of the samples that faces the autoclave walls for the subsequent analysis because they are exposed to the highest flow fields. According to the CFD results, the average flow rate and the average wall shear stress on the outer surface of the samples after spinning them at 600, 300, 180 and 90 rpm were 0.94, 0.47, 0.28, 0.14 m/s and 0.133, 0.036, 0.015, 0.005 Pa, respectively.

#### ***3.2 Droplet displacement theory***

Regardless of the water condensation mechanism operating, at any given time the steel samples inside the autoclave are expected to be covered by a distribution of water droplets with different sizes. Their size distribution is controlled by the nucleation and growth rate (condensation rate) and by the forces acting on them (such as: gravity, drag and centrifugal forces), that may lead to their removal from the surface.

In Zhang et al.'s [12] mechanistic droplet formation model, the dropwise condensation is based on heat and mass-transfer, because the water condensing of the surface must come from the gas phase and pass through the mass-transfer boundary layer before it can get to the surface. Therefore, it is expected that an increase in mass transfer/flow rate would increase the condensation rate (nucleation and growth of water droplets). The same model also allows the calculation of the lifetime, or critical radius, of the droplets before they slide away, fall down or detach from a surface based on the forces acting on its volume (Figure 6). All the forces shown are a function of the droplet diameter, but they increase at different rates. For small droplets the forces that hold it in place (surface tension and friction) are much larger than the others, so the droplet remains stationary on the surface. As the droplet grows due to condensation, the forces that are proportional to the volume increase faster, until a critical size is reached, at which the droplet will begin to move. This critical size represents the lifetime of a droplet and can be calculated using Zhang et al.'s [12] model, where, as soon as one of the conditions is met the droplet will move along the x (detach), y (slide away) or z (fall down) axis. [12]

Figure 7 shows the critical water droplet size as a function of the supercritical CO<sub>2</sub> velocity for droplets sitting on the surface of the sample facing the outer of the rotating cage at 35 °C and 80 bar. Under the experimental conditions considered, the droplet lifetime is expected to end due to the gravity (fall down) at low velocities or due to the drag force (slide away) at high velocities. Taking this scenario into account, the distribution of water droplets on the surface should be barely affected by low velocities (<0.34 m/s), but for higher velocities (>0.34 m/s) the average droplet size observed should decrease, contributing to a reduction of the overall wetted area. However, the condensation rate is expected

to increase for higher velocities due to the increase in mass transfer of water vapour to the surface. These two opposing mechanisms make it difficult to estimate the overall effect on the wetted area.

### **3.3 The effect of the flow on the corrosion rate**

Figure 8 shows the calculated corrosion rates determined from mass loss measurements in autoclave tests carried out at 35 °C, 80 bar and exposed to distinct flow rate conditions for 48 h. No substantial difference in corrosion rate was observed between the samples of the tests carried out under dynamic conditions:  $0.049 \pm 0.018$ ,  $0.081 \pm 0.021$ ,  $0.061 \pm 0.006$ ,  $0.065 \pm 0.020$  mm/y for the tests carried out at 0.15, 0.3, 0.5 and 1 m/s, respectively. This indicates that under these conditions it is likely that the average droplet size is much smaller than the critical size. Therefore, the forces acting on the droplets volume due to the supercritical CO<sub>2</sub> flow are less than the minimum required to affect the droplet size distribution on the surface.

However, the corrosion rate measured under static conditions (0.207 mm/year) was 3-4 times higher than those observed under dynamic conditions. Assuming that during the initial stage, the corrosion rate is proportional to the wet area [1,8,9], this corrosion rate measurement would indicate that the water wetting was more extensive on the samples tested in static condition. Morland and Svenningsen [24] reported that wetting of the surface may happen in the initial step of the test setup and that condensation of water droplets may occur during the depressurisation of the test systems at the end of experiments can contribute to misleading corrosion rates. However, since all the tests in this study followed the same setup and stop procedure, they can be readily compared.

In order to test the wetting of the surface in the initial step of the test setup hypothesis, either due to accidental splashing of the water located at the bottom of the autoclave, caused by the injection of CO<sub>2</sub> or condensation that may have happened during decompression step of the purge to remove oxygen from the autoclave, it was decided to repeat the static test, but letting it rotate at the maximum speed (600 rpm) for 1 h at the beginning of the test to displace the droplets that may eventually form during the test setup. In this particular test the measured corrosion rate was 0.069 mm/year, analogous to those observed under dynamic conditions, which might indicate that splashing of the sample can be an inherent problem when charging the autoclave.

### **3.4 Analysis of corrosion product morphology**

Figure 9 displays SEM images of corroded X80 steel samples exposed to water-saturated supercritical CO<sub>2</sub> phase at distinct velocity fields. It shows a steel surface almost fully covered by a thin layer of corrosion product on the sample tested under static conditions. As the rotating speed increases, the corrosion product does not form a continuous layer anymore, instead, thin patches can be observed. Similar morphologies have been observed by previous studies in similar conditions [25,26].

The corrosion in supercritical CO<sub>2</sub> systems is expected to occur in the wetted areas, leaving a footprint of corrosion features (patches) indicating the areas that were wetted during the tests. Therefore, it was reasonable to assume the area of those patches as the area of a hemispherical droplet that was present there during the test. Research into the displacement of liquid droplets on a surface by a shearing air flow was performed by Fan et al. [27]. Their research indicated three modes of droplet motion: (i) the droplets retaining the shape during motion, (ii) droplets developing a tail that moves at the same speed and (iii) the tail breaking up to form smaller droplets. The absence of signs of droplet tail found in the SEM images, indicates that if any motion is happening during the test, it is likely of type (i).

Figure 10 shows the droplet size distribution on the surface of the X80 samples tested in water-saturated supercritical CO<sub>2</sub> at 80 bar and 35 °C exposed to various flow rates for 48 h. It shows that the flow velocity (up to 1 m/s) barely affected the size distribution of corrosion product scale on the surface of the samples. It also shows an average droplet size two orders of magnitude smaller than the calculated critical size shown in Figure 7, indicating that the droplets are not expected to be displaced by the tested flow conditions and should remain stationary on the surface.

Upon closer inspection, the SEM images (Figure 11) revealed that the morphology of the corrosion product patches observed previously on X80 steel exposed to the water-saturated supercritical CO<sub>2</sub> at 35 °C for 48 h under different flow conditions consisted of stacked cubic crystals. Additionally, focused ion beam (FIB) was used to cut a slice of the corrosion product patches, allowing a cross-section analysis, as shown in the SEM in Figure 12. An energy dispersive X-ray (EDX) elemental analysis of this area was carried out, indicating that the film consisted mainly of iron, oxygen and carbon. The morphology and the elemental distributions of the corrosion product scale demonstrated that this layer consisted of iron carbonate (FeCO<sub>3</sub>). This is consistent with previous observations in the literature from tests carried out in similar conditions [11,25,26,28]. In addition, the FeCO<sub>3</sub> layer was observed to have a thickness of approximately 5 µm.

To supplement the surface analysis data, profilometry measurements were made to assess the extent of pitting. For each test one sample was selected for the scan, Figure 13 shows examples of the profilometry measurements taken from the samples exposed to the water-saturated supercritical CO<sub>2</sub> at 35 °C for 48 h under different flow conditions. For each of those samples, three 1x1 mm<sup>2</sup> areas were randomly scanned on the surface. The pits in the combined three areas for each sample were measured, then the Eq. 2 was used to assess the extent of the pitting damage, and the result is shown in Figure 14.

The results show that in water-saturated supercritical CO<sub>2</sub> at 80 bar and 35 °C, the average pitting rate was 0.59±0.13, 0.55±0.15, 0.59±0.09, 0.76±0.16 and 0.70±0.17 mm/y for the tests carried out under 0, 0.15, 0.3, 0.5 and 1 m/s flow rates, respectively. The maximum pit depth measured were akin to the corrosion product layer thickness observed using FIB/SEM. However, the calculated pit penetration rates (Eq. 2) are up to one order of magnitude higher than the uniform corrosion rates obtained through mass loss tests. Which suggests that the corrosion rates calculated from mass loss measurements may not be accurate in terms of assessing the true threat associated with the corrosion process. These results are in accordance with the observations by Farelas et al. [29] and Hua et al. [30], who carried out tests in static conditions at 80 bar in liquid CO<sub>2</sub> at 25 °C and supercritical CO<sub>2</sub> at 35 °C, respectively. Both results presented in this paper and the previous results from the literature indicate that mass loss tests may underestimate the risk represented by pitting corrosion of carbon steel in supercritical CO<sub>2</sub>, even in the absence of impurities. But, despite that, it is also worth mentioning that the results indicate that, just as observed in the uniform corrosion measurements, the presence of a supercritical CO<sub>2</sub> flow has no significant effect on the pit penetration rate within the range studied

## 4 CONCLUSIONS

In this study the effect of the water-saturated supercritical CO<sub>2</sub> flow rate on the corrosion behaviour of X80 steel at a temperature of 35 °C and pressure of 80 bar was investigated.

- The uniform general corrosion rate of X80 steel in water-saturated supercritical CO<sub>2</sub> environments was not enhanced in the presence of a fluid flow. No substantial difference in uniform general corrosion rate was observed between the X80 samples tested under conditions up to 1 m/s.

- The size of the corrosion patches on the surface of the samples, which were assumed as being the size of the condensed water droplets, were two orders of magnitude smaller than the calculated critical droplet size. Therefore, the drag force generated by the scCO<sub>2</sub> flow was below the threshold required to displace the observed droplets size on the steel surface.
- The measured pitting penetration rates were up to one order of magnitude higher than the uniform corrosion rates obtained through mass loss tests, indicating that it may represent a potential concern for the integrity of carbon steel pipelines used in CO<sub>2</sub> transportation and injection conditions.

## 5 ACKNOWLEDGMENTS

The authors would like to acknowledge the funding from CNPq (National Council for Scientific and Technological Development/Brazil) and Shell (Brazil), which made this research possible. This work was also partly undertaken on ARC4, part of the High-Performance Computing facilities at the University of Leeds. The authors would like to thank the technical support from the Institute of functional Surfaces at the University of Leeds.

## 6 REFERENCES

1. Liu, A.Q., C. Bian, Z.M. Wang, X. Han, and J. Zhang, *Corros. Sci.* 134 (2018): pp. 149–161, <https://doi.org/10.1016/j.corsci.2018.02.027>.
2. Allinson, K., D. Burt, L. Campbell, L. Constable, M. Crombie, A. Lee, V. Lima, T. Lloyd, and L. Solsbey, *Energy Procedia* 114 (2017): pp. 6950–6956, <http://dx.doi.org/10.1016/j.egypro.2017.03.1837>.
3. Barker, R., Y. Hua, and A. Neville, *Int. Mater. Rev.* 62 (2017): pp. 1–31, <https://doi.org/10.1080/09506608.2016.1176306>.
4. Sim, S., I.S. Cole, Y.S. Choi, and N. Birbilis, *Int. J. Greenh. Gas Control* 29 (2014): pp. 185–199, <http://dx.doi.org/10.1016/j.ijggc.2014.08.010>.
5. Wei, L., Y. Zhang, X. Pang, and K. Gao, *Corros. Rev.* 33 (2015): pp. 151–174, <https://doi.org/10.1515/correv-2014-0067>.
6. Wei, L., X. Pang, and K. Gao, *Corros. Sci.* 136 (2018): pp. 339–351, <http://doi.org/10.1016/j.corsci.2018.03.020>.
7. Zhang, G.A., D. Liu, Y.Z. Li, and X.P. Guo, *Corros. Sci.* 120 (2017): pp. 107–120, <http://dx.doi.org/10.1016/j.corsci.2017.02.012>.
8. Xiang, Y., C. Li, W. Hesitao, Z. Long, and W. Yan, *J. Supercrit. Fluids* 138 (2018): pp. 132–142, <https://doi.org/10.1016/j.supflu.2018.04.009>.
9. Jiang, X., D. Qu, X. Song, X. Liu, and Y. Zhang, *Int. J. Greenh. Gas Control* 85 (2019): pp. 11–22, <https://doi.org/10.1016/j.ijggc.2019.03.020>.
10. Xiang, Y., Z. Wang, M. Xu, Z. Li, and W. Ni, *J. Supercrit. Fluids* 82 (2013): pp. 1–12, <http://dx.doi.org/10.1016/j.supflu.2013.05.016>.
11. Choi, Y.S., and S. Nešić, *Int. J. Greenh. Gas Control* 5 (2011): pp. 788–797, <http://doi.org/10.1016/j.ijggc.2010.11.008>.
12. Zhang, Z., D. Hinkson, M. Singer, H. Wang, and S. Nesic, “A Mechanistic Model of Top of the Line Corrosion,” in *Corros. 2007* (2007).
13. Lee, C.T., P.A. Psathas, K.P. Johnston, J. DeGrazia, and T.W. Randolph, *Langmuir* 15 (1999): pp. 6781–6791, <https://doi.org/10.1021/la9903548>.
14. Spycher, N., K. Pruess, and J. Ennis-King, *Geochim. Cosmochim. Acta* 67 (2003): pp. 3015–3031, [https://doi.org/10.1016/S0016-7037\(03\)00273-4](https://doi.org/10.1016/S0016-7037(03)00273-4).
15. ASTM G1-03, “Standard Practice for Preparing, Cleaning, and Evaluation Corrosion Test Specimens,” ASTM International (2003).
16. Schindelin, J., I. Arganda-Carreras, E. Frise, V. Kaynig, M. Longair, T. Pietzsch, S. Preibisch, C. Rueden, S. Saalfeld, B. Schmid, J.Y. Tinevez, D.J. White, V. Hartenstein, K. Eliceiri, P. Tomancak, and A. Cardona, *Nat. Methods* 9 (2012): pp. 676–682, <https://doi.org/10.1038/nmeth.2019>.

17. Wei, L., X. Pang, and K. Gao, *Corros. Sci.* 103 (2016): pp. 132–144, <https://doi.org/10.1016/j.corsci.2015.11.009>.
18. Multiphysics, C., *COMSOL Multiphysics* (2016): p. 598.
19. Batchelor, G.K., *An Introduction to Fluid Dynamics* (Cambridge University Press, 2000).
20. Wilcox, D.C., *Turbulence Modeling for CFD*, 3rd ed. (DCW Industries Inc, 2006).
21. Bahadori, A., H.B. Vuthaluru, and S. Mokhatab, *Int. J. Greenh. Gas Control* 3 (2009): pp. 474–480, <https://doi.org/10.1016/j.ijggc.2009.01.003>.
22. Heidaryan, E., T. Hatami, M. Rahimi, and J. Moghadasi, *J. Supercrit. Fluids* 56 (2011): pp. 144–151, <http://dx.doi.org/10.1016/j.supflu.2010.12.006>.
23. Kumar, A., S. Ling, J.L. Pacheco, S.K. Desai, and R. V. Reddy, “Effects of Rotating Cage Autoclave Design on Shear Stress and Flow Pattern,” in *Corros. 2013* (2013), pp. 1–13.
24. Morland, B.H., and G. Svenningsen, “Pitfalls and Artefacts in Corrosion Experiments with Dense Phase CO<sub>2</sub>,” in *Corros. 2021* (2021).
25. Hua, Y., R. Barker, T. Charpentier, M. Ward, and A. Neville, *J. Supercrit. Fluids* 98 (2015): pp. 183–193, <http://dx.doi.org/10.1016/j.supflu.2014.12.009>.
26. Hua, Y., R. Barker, and A. Neville, *Int. J. Greenh. Gas Control* 31 (2014): pp. 48–60, <http://dx.doi.org/10.1016/j.ijggc.2014.09.026>.
27. Fan, J., M.C.T. Wilson, and N. Kapur, *J. Colloid Interface Sci.* 356 (2011): pp. 286–292, <http://dx.doi.org/10.1016/j.jcis.2010.12.087>.
28. Hua, Y., R. Barker, and A. Neville, *J. Supercrit. Fluids* 97 (2015): pp. 224–237, <http://dx.doi.org/10.1016/j.supflu.2014.12.005>.
29. Farel, F., Y.S. Choi, and S. Nestic, “Effects of CO<sub>2</sub> Phase Change, SO<sub>2</sub> Content and Flow on the Corrosion of CO<sub>2</sub> Transmission Pipeline Steel,” in *Corros. 2012* (2012), pp. 2538–2553.
30. Hua, Y., R. Barker, and A. Neville, *Corrosion* 71 (2015): pp. 667–683, <https://doi.org/10.5006/1504>.

## 7 FIGURE CAPTIONS

FIGURE 1. (a) Schematic diagram of the test setup and (b) detail showing the samples attached to the holder and rotating shaft.

FIGURE 2. Steps of the image processing, (a) raw unprocessed image, (b) feature selection, (c) segmentation and (d) feature analysis.

FIGURE 3. (a) Geometry of the CFD model used to simulate fluid flow and (b) sketch of the problem set-up on a horizontal section.

FIGURE 4. (a) Horizontal section of the mesh showing region adjacent to the sample and (b) mesh sensitivity study showing the predicted velocity 0.5 mm ahead of the sample leading surface as a percentage accuracy compared to the predicted velocity at the same position using the most refined mesh.

FIGURE 5. CFD simulation velocity field results at different rotating speeds of (a and b) 90 rpm (0.15 m/s), (c and d) 180 rpm (0.3 m/s), (e and f) 300 rpm (0.5 m/s) and (g and h) 600 rpm (1.0 m/s) at horizontal mid-plane of the samples. Arrows indicate flow direction.

FIGURE 6. Force analysis on a single droplet.  $F_c^x$ : centrifugal force;  $F_\gamma^x$ : surface tension force;  $F_d^y$ : flow drag force;  $F_b^z$ : buoyancy;  $F_g^z$ : gravity force;  $F_a^y$  and  $F_a^z$ : friction force between the liquid droplet and the solid wall.

FIGURE 7. Critical droplet size as a function of the supercritical CO<sub>2</sub> velocity for the proposed test setup at 35 °C and 80 bar.

FIGURE 8. Variation of the corrosion rate of X80 steel immersed in water-saturated supercritical CO<sub>2</sub> at 35 °C and 80 bar after 48 h of immersion with increasing flow rate.

FIGURE 9. Surface morphologies of the corrosion products on X80 steel immersed in water-saturated supercritical CO<sub>2</sub> at 80 bar and 35 °C exposed to flow rates of (a) 0 m/s, (b) 0.15 m/s, (c) 0.3 m/s, (d) 0.5 m/s and (e) 1.0 m/s for 48 h and (f) fast initial rotation for short period then 0 m/s (47 h).

FIGURE 10. Droplet size distribution on the surface of the X80 samples tested in water-saturated supercritical CO<sub>2</sub> at 80 bar and 35 °C exposed to flow rates of (a) 0.15 m/s, (b) 0.3 m/s, (c) 0.5 m/s and (d) 1.0 m/s for 48 h.

FIGURE 11. SEM morphology of the corrosion patches on X80 steel immersed in water-saturated supercritical CO<sub>2</sub> at 80 bar and 35 °C exposed to a flow rate of 1.0 m/s for 48 h.

FIGURE 12. SEM image showing the location where the corrosion product layer was sliced using the FIB and an EDX analysis for the corrosion product layer area highlighted in red.

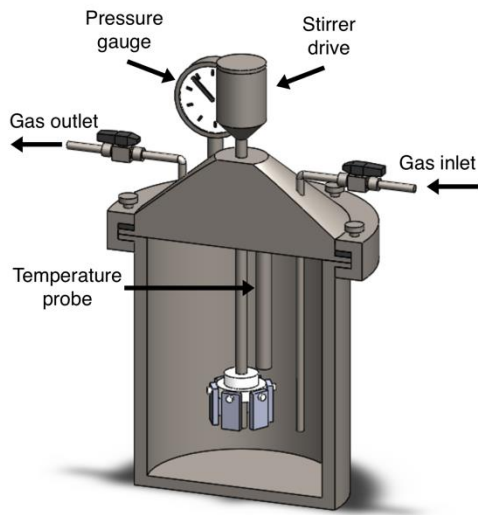
FIGURE 13. Surface profilometry of an area in the centre of the outer surface of the samples after testing at 80 bar and 35 °C exposed to flow rates of (a) 0 m/s, (b) 1.0 m/s for 48 h and then cleaned with Clarke solution.

FIGURE 14. Variation of the pitting penetration rate of X80 steel immersed in water-saturated supercritical CO<sub>2</sub> at 35 °C and 80 bar after 48 h of immersion at different flow rates.

## 8 TABLES

TABLE 1. Test matrix for corrosion tests in water-saturated supercritical CO<sub>2</sub>.

Temperature (°C)	Pressure (bar)	Flow rate (m/s)	Test duration (h)
35	80	0	48
		0.15	
		0.3	
		0.5	
		1.0	
		1.0 (1h) then 0 (47h)	

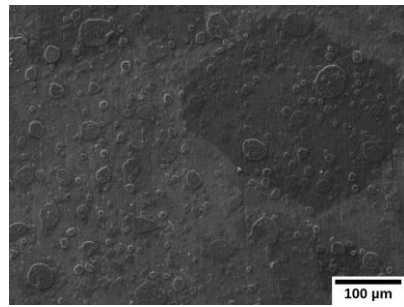


(a)

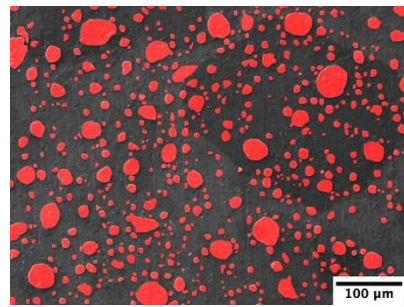


(b)

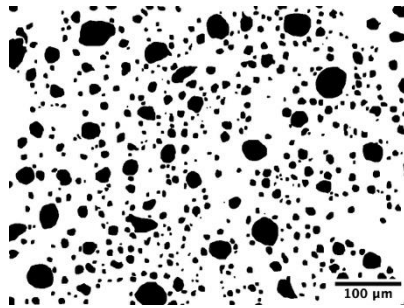
FIGURE 1. (a) Schematic diagram of the test setup and (b) detail showing the samples attached to the holder and rotating shaft.



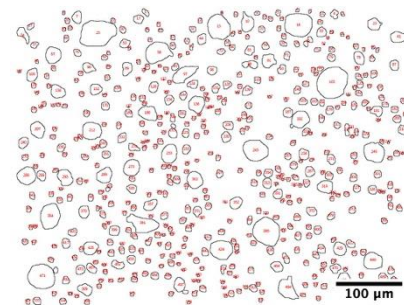
(a)



(b)



(c)



(d)

FIGURE 2. Steps of the image processing, (a) raw unprocessed image, (b) feature selection, (c) segmentation and (d) feature analysis.

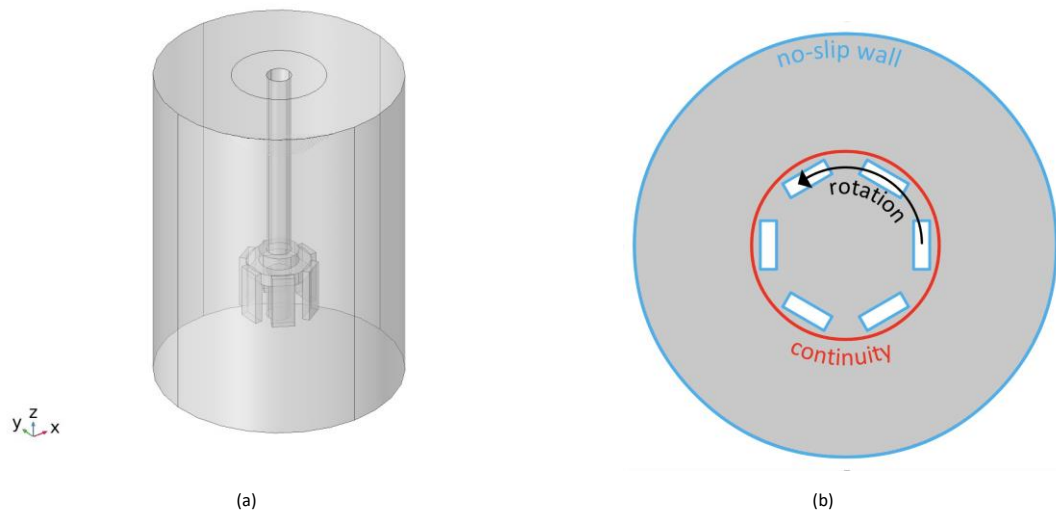


FIGURE 3. (a) Geometry of the CFD model used to simulate fluid flow and (b) sketch of the problem set-up on a horizontal section.

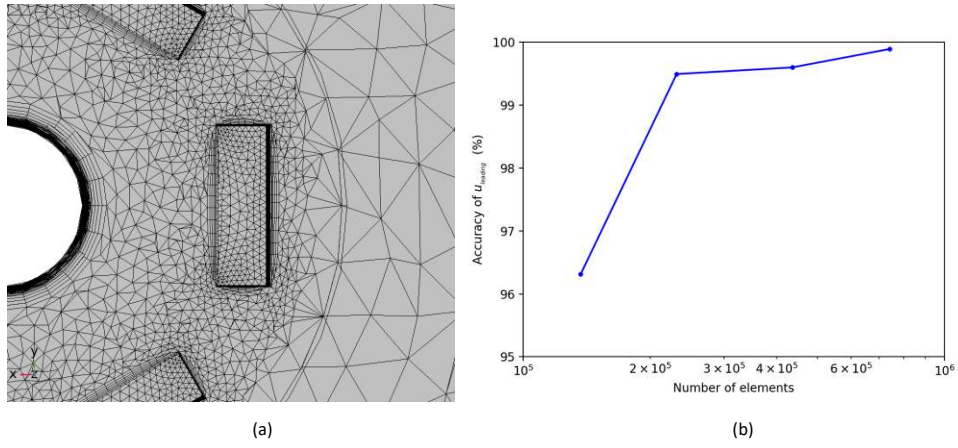


FIGURE 4. (a) Horizontal section of the mesh showing region adjacent to the sample and (b) mesh sensitivity study showing the predicted velocity 0.5 mm ahead of the sample leading surface as a percentage accuracy compared to the predicted velocity at the same position using the most refined mesh.

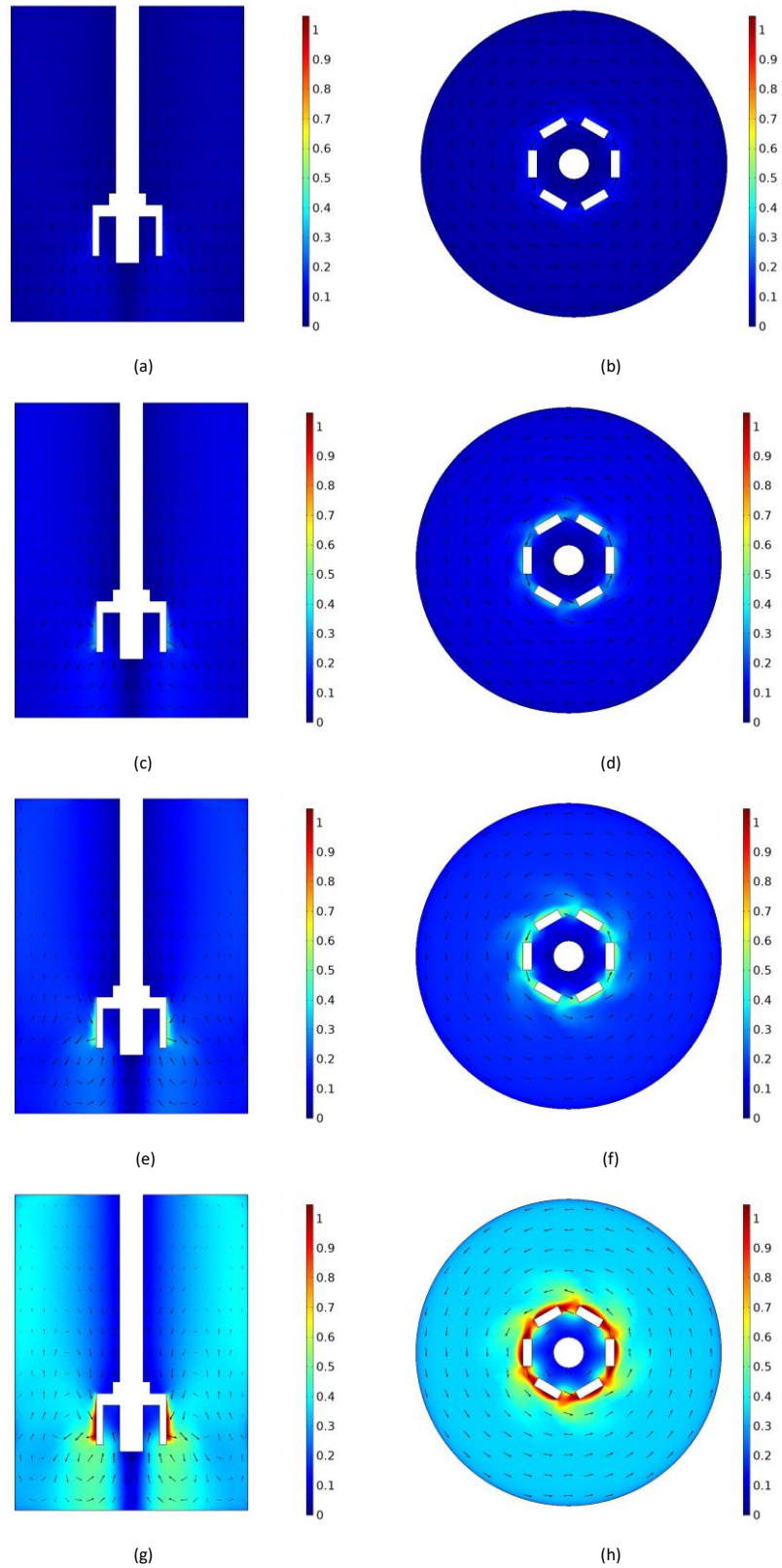


FIGURE 5. CFD simulation velocity field results at different rotating speeds of (a and b) 90 rpm (0.15 m/s), (c and d) 180 rpm (0.3 m/s), (e and f) 300 rpm (0.5 m/s) and (g and h) 600 rpm (1.0 m/s) at horizontal mid-plane of the samples. Arrows indicate flow direction.

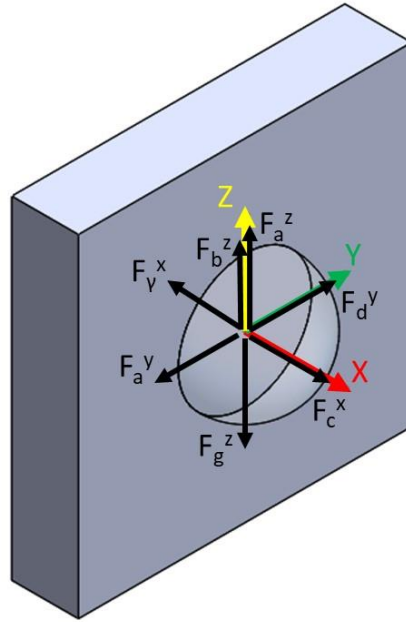


FIGURE 6. Force analysis on a single droplet.  $F_c^x$ : centrifugal force;  $F_v^x$ : surface tension force;  $F_d^y$ : flow drag force;  $F_b^z$ : buoyancy;  $F_g^z$ : gravity force;  $F_a^y$  and  $F_a^z$ : friction force between the liquid droplet and the solid wall.

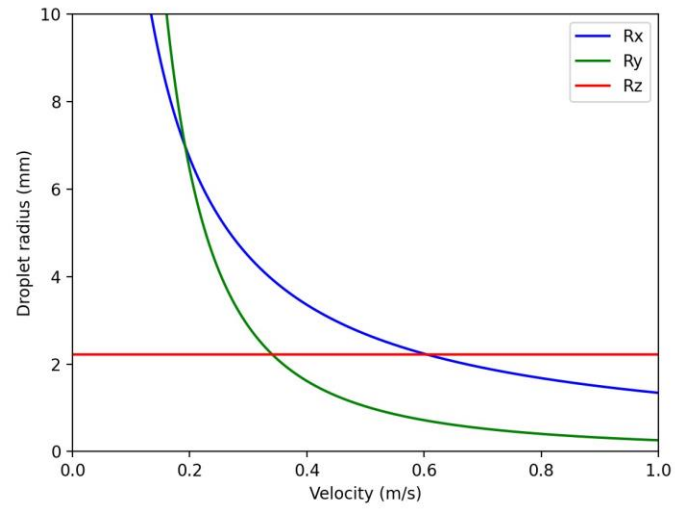


FIGURE 7. Critical droplet size as a function of the supercritical CO<sub>2</sub> velocity for the proposed test setup at 35 °C and 80 bar.

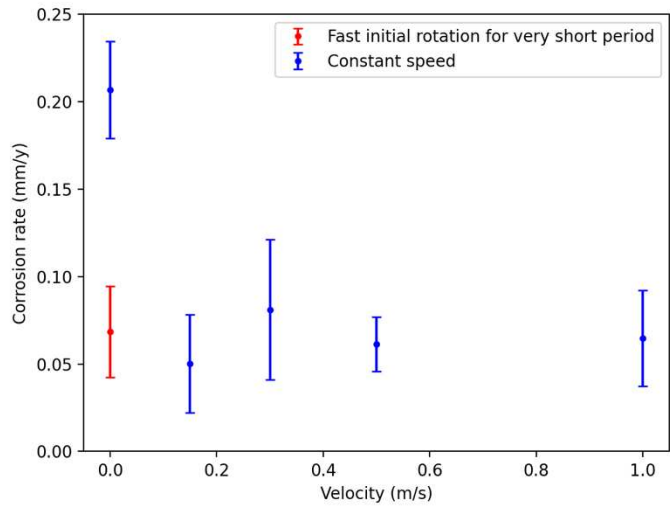


FIGURE 8. Variation of the corrosion rate of X80 steel immersed in water-saturated supercritical CO<sub>2</sub> at 35 °C and 80 bar after 48 h of immersion with increasing flow rate.

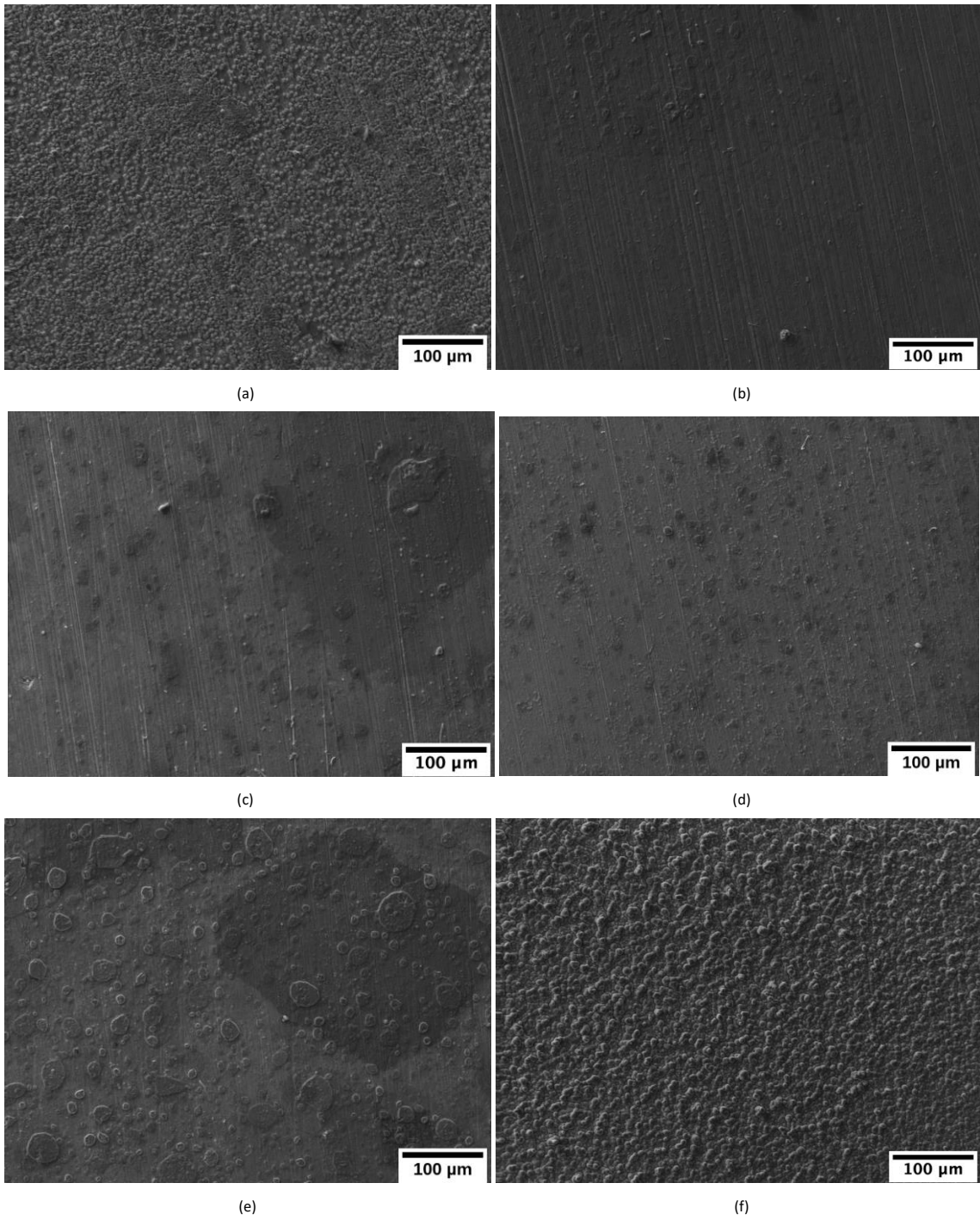
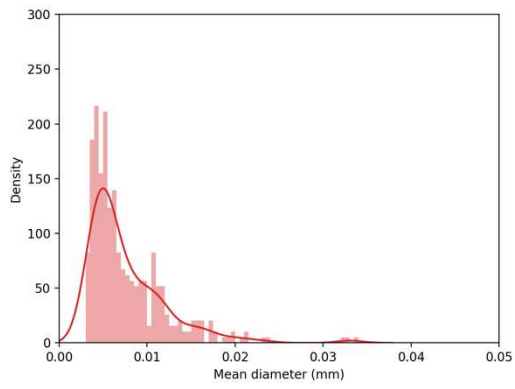
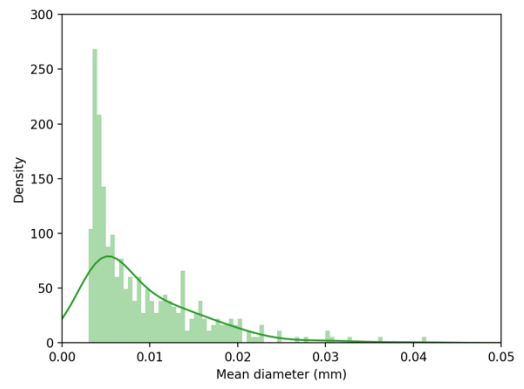


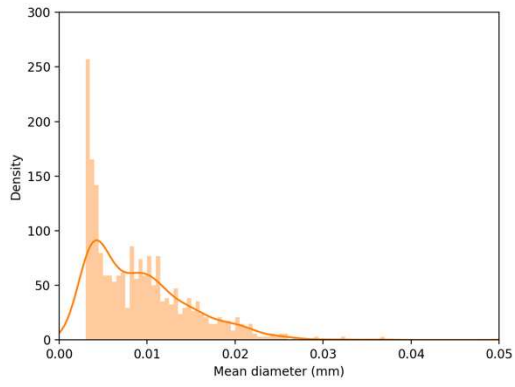
FIGURE 9. Surface morphologies of the corrosion products on X80 steel immersed in water-saturated supercritical CO<sub>2</sub> at 80 bar and 35 °C exposed to flow rates of (a) 0 m/s, (b) 0.15 m/s, (c) 0.3 m/s, (d) 0.5 m/s and (e) 1.0 m/s for 48 h and (f) fast initial rotation for short period then 0 m/s (47 h).



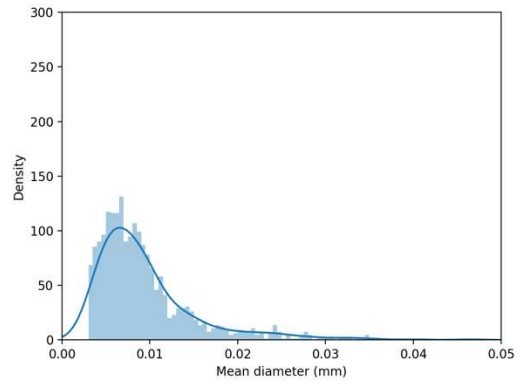
(a)



(b)



(c)



(d)

FIGURE 10. Droplet size distribution on the surface of the X80 samples tested in water-saturated supercritical CO<sub>2</sub> at 80 bar and 35 °C exposed to flow rates of (a) 0.15 m/s, (b) 0.3 m/s, (c) 0.5 m/s and (d) 1.0 m/s for 48 h.

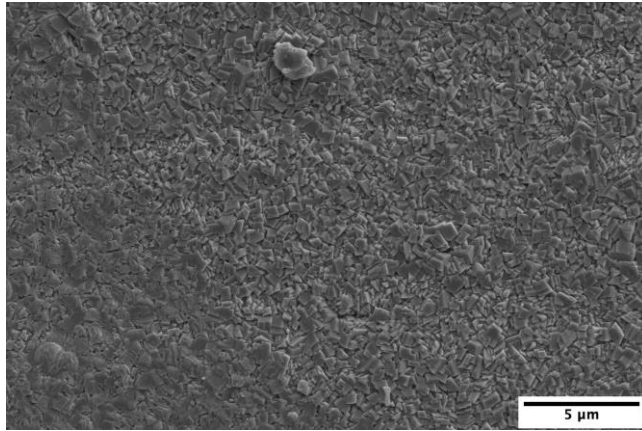


FIGURE 11. SEM morphology of the corrosion patches on X80 steel immersed in water-saturated supercritical CO<sub>2</sub> at 80 bar and 35 °C exposed to a flow rate of 1.0 m/s for 48 h.

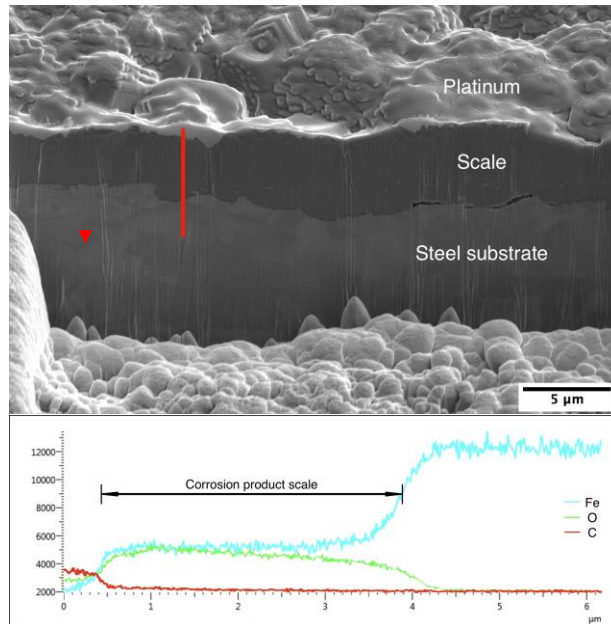


FIGURE 12. SEM image showing the location where the corrosion product layer was sliced using the FIB and an EDX analysis for the corrosion product layer area highlighted in red.

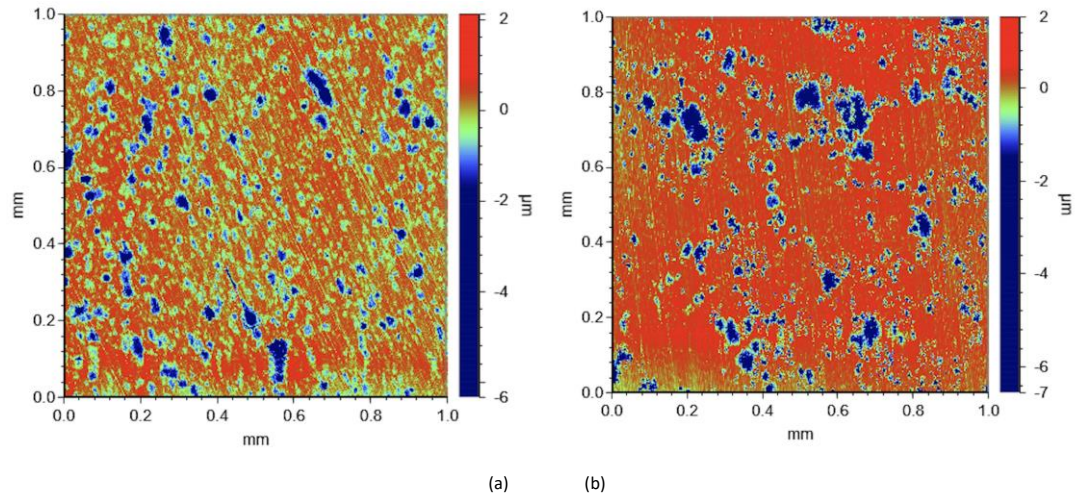


FIGURE 13. Surface profilometry of an area in the centre of the outer surface of the samples after testing at 80 bar and 35 °C exposed to flow rates of (a) 0 m/s, (b) 1.0 m/s for 48 h and then cleaned with Clarke solution.

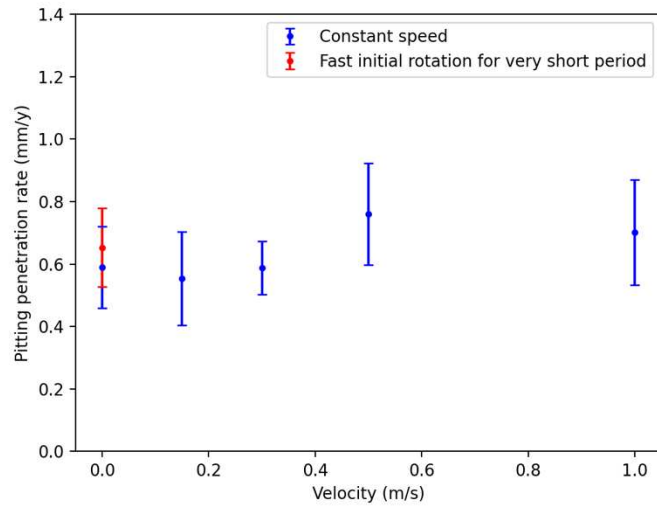


FIGURE 14. Variation of the pitting penetration rate of X80 steel immersed in water-saturated supercritical CO<sub>2</sub> at 35 °C and 80 bar after 48 h of immersion at different flow rates.